Temperature-Dependent Polarization in Field-Effect Transport and Photovoltaic Measurements of Methylammonium Lead Iodide

John G. Labram,[1,3] *Douglas H. Fabini,*[2,3] *Erin E. Perry,*[1,3] *Anna J. Lehner,*[2,3] *Hengbin Wang,*[3] *Anne M. Glaudell,*[1] *Guang Wu,*[4] *Hayden Evans,*[2,3] *David Buck,*[5] *Robert Cotta,*[5] *Luis Echegoyen,*[5] *Fred Wudl,*[1,2,3] *Ram Seshadri,*[1,2,3] *Michael L. Chabinyc*[1,2,3*]

[1]University of California Santa Barbara, California NanoSystems Institute (CNSI), Santa Barbara, CA 93106 USA

[2]University of California Santa Barbara, Materials Research Laboratory, Santa Barbara, CA 93106 USA

[3]University of California Santa Barbara, Mitsubishi Chemical - Center for Advanced Materials, Santa Barbara, CA 93106 USA

[4]University of California Santa Barbara, Department of Chemistry & Biochemistry, Santa Barbara, CA 93106 USA

[5]University of Texas El Paso, Department of Chemistry, El Paso, TX 79968 USA

*Corresponding Author: Michael Chabinyc, Materials Department, University of California, Santa Barbara CA 93106-5050, email: mchabinyc@engineering.ucsb.edu

ABSTRACT:

While recent improvements in the reported peak power conversion efficiency (PCE) of hybrid organic-inorganic perovskite solar cells have been truly astonishing, there are many fundamental questions about the electronic behavior of these materials. Here we have studied a set of electronic devices employing methylammonium lead iodide ($(MA)PbI_3$) as the active material and conducted a series of temperature-dependent measurements. Field-effect transistor, capacitor and photovoltaic cell measurements all reveal behavior consistent with substantial and strongly temperature-dependent polarization susceptibility in $(MA)PbI_3$ at temporal and spatial scales that significantly impact functional behavior. The relative PCE of $(MA)PbI_3$ photovoltaic cells is observed to reduce drastically with decreasing temperature, suggesting that such polarization effects could be a prerequisite for high-performance device operation.

TOC GRAPHIC

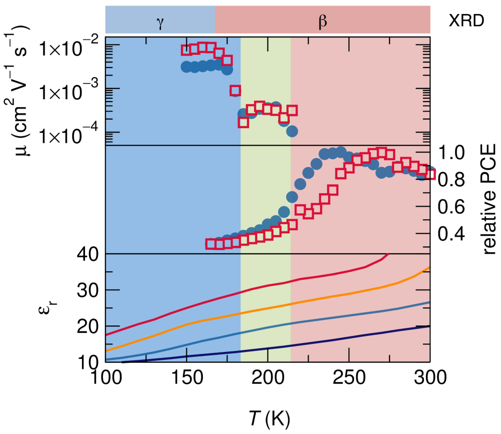

KEYWORDS: Hybrid Halide Perovskite, Ionic Motion, Polarization, $(MA)PbI_3$, Transistors, Low-Temperature

The pace at which new materials and designs for solar cells emerge is very slow,[1-6] and is arguably comparable to the discovery of high T_c superconductors.[7-8] The finding that hybrid organic metal halide solar cells based on $CH_3NH_3PbI_3$ can lead to high power conversion efficiency (PCE) using simple coating methods, in a material comprising earth-abundant elements has therefore garnered significant interest.[6, 9-10] Not only has the peak reported PCE exceeded 20% in a short time,[11-13] but the processing techniques widely employed suggest that commercial products could be fabricated using low-cost, large-area techniques, potentially compatible with flexible substrates.[14]

The ABX_3 perovskite crystal structure is characterized by three-dimensionally corner connected network of $BX_{6/2}$ octahedra that is filled by the A ions. Perovskite compounds where the A is an organic cation, B is usually a main group element, and X is a group 7 anion (halide) are referred to as hybrid organic-inorganic or hybrid-halide perovskites. Materials in this class are found to possess strong optical absorption,[6, 15] impressive electrical properties[16] and an unusually low density of trap states,[17] resulting in the demonstration of solar cells with remarkably high reported PCEs.[6, 9, 11, 13-14] In spite of the progress made in forming solar cells, there are many fundamental questions about the properties of the organic metal halide materials systems that enable this performance. Hybrid organic-inorganic perovskite solar-cells are notable for their various instabilities and measurement-dependent behavior.[18-25] These instabilities vary widely between device structures due to different processing methods, such as growth in ambient or in controlled atmospheres, and due to measurement conditions. The origins of this behavior are generally attributed to a variety of mechanisms including mass diffusion of ions,[25-27] structural changes,[28] and grain boundaries.[29]

While there has been intense effort directed at understanding the optoelectronic performance of organic metal halide materials, there has been less work to understand their properties more broadly as semiconductors. Work by Mitzi and co-workers had demonstrated field effect devices in Sn-based compounds with layered structures some years ago.[30] Despite high reported carrier mobilities,[16] easily-accessible conduction and valence band energies[31] and previous reports employing other hybrid perovskites,[30] field-effect transistors (FETs) based on methylammonium lead iodide ($(MA)PbI_3$) have, until very recently,[32] remained notably absent from the literature.

A number of studies have considered the possibility that ionic migration[18, 20, 25-27, 33] or ferroelectric polarization[34-36] are pertinent processes in perovskite solar cells, though substantial debate remains.[37] Ionic migration has been observed in a number of oxide and halide materials adopting the perovskite structure,[38-42] and has recently been studied experimentally and computationally in $(MA)PbI_3$.[26, 33] Here we have fabricated a set of electronic devices based on $(MA)PbI_3$ in order to study the nature of electrical instabilities in this system. By measuring the electrical characteristics of FETs, capacitors and solar cells as a function of temperature, we observe behavior consistent with a substantial susceptibility to polarization, potentially due to ionic mass transport within thin films of $(MA)PbI_3$.

To examine the electrical behavior of thin films of $(MA)PbI_3$ we fabricated bottom-gate, top-contact (BGTC) FETs (see inset to Figure 1(a)). The $(MA)PbI_3$ was deposited using recently reported[12, 43] solvent-annealing techniques, as applied to planar-architecture PV cells. A solution of $(MA)PbI_3$ was formed from a 1:1 molar ratio of lead iodide (PbI_2) and CH_3NH_3I. The solution was deposited via spin-casting in ambient-pressure N_2, and chlorobenzene (which does not dissolve $(MA)PbI_3$) was applied to the film during the spin-casting process. More details are provided in the Supporting Information.

We found that the electrical characteristics of $(MA)PbI_3$ had a complex temperature dependence. At room temperature these devices exhibit low source-drain currents and no field-induced current modulation (see Figure 1(a)). However when the temperature is reduced below 220K, a field-effect is observed and the drain current continues to increase as the temperature is reduced. Where the drain current is observed to be substantially in excess of gate current the gradual-channel approximation[44] has been applied to extract a value of field-effect mobility. The gradual channel approximation for extraction of carrier mobility in field-effect devices assumes a single electronic charge carrier, uniform carrier accumulation in the channel, and time-independent behavior and consequently does not provide a simple estimation of the carrier motion for measurements with non-ideal effects. This is consistent with our observation of absolute values of electron mobility substantially lower than those previously reported using other techniques.[16] Nonetheless it can be applied as a proxy for relative transistor performance, assuming a high transconductance is desirable. Since aluminum source and drain electrodes have been employed here, only electron transport is observed. This is as one would expect given the position of the valence band and conduction band energies of $(MA)PbI_3$ relative to the work function of aluminum.[31] As shown in Figure 1(b) a roughly temperature-independent value is observed, with the exception of an approximately one order of magnitude change in mobility around 180K. Above 215K the drain current was too low to apply the gradual-channel approximation and these points have not been plotted.

If $(MA)PbI_3$ exhibits substantial polarization susceptibility (via mobile ions or alignment of the dipolar molecular cation, for example) one would expect the application of an electric field to result in the absorption of energy by the structure, and an electronic screening effect in electronic devices (see Figure 1(c)).[33] Such a mechanism should be expected to result in a screening of applied gate fields in FETs and hence inhibit accumulation of carriers and the electrical conductivity of the channel. Both the diffusion of ionic species and polarization due to local molecular motion in the solid are expected to be temperature-activated.[33-34, 45] For this reason one should expect that over the time-scales relevant for measurement of field effect conduction (typically 10's of ms to 1s per data point), the screening mechanism can be strongly suppressed by reducing the temperature of the device. The larger aliphatic or aromatic (di)ammonium cations employed in previously-reported hybrid halide FETs[30] led to a 2D layered structure rather than the 3D structure of (MA)PbI_3. It is likely that these larger cations are less mobile than methylammonium cations, which could consequently lead to a substantially diminished screening effect if this species is indeed responsible for the observed behavior.

These observations are consistent with temperature-dependent dielectric properties or temperature-activated ionic migration. The temperature-independence of mobility below 210K (aside from the discontinuity in mobility at 180K) is attributed to two competing effects. Charge transport in polycrystalline and disordered semiconductors is described by temperature-activated processes[46] and hence one should expect to observe a reduced carrier mobility with lower temperature. However as described above, over the time-scales relevant for electrical measurements, screening effects are expected to inhibit charge transport in transistor devices and can hence be expected to lead to an increased observed mobility with reducing temperature as the effect of screening is reduced. The convolution of these two phenomena is expected to be complex and it is hence difficult to make detailed *a-priori* predictions on the temperature-dependence of apparent mobility in this system. The reason behind the observed change in mobility between 175K and 185K is unclear. There exists a known structural phase transition in (MA)PbI$_3$ at a temperature of 163K.[16, 47] The structure is found to change phase from tetragonal (β) above 163K to orthorhombic (γ) below 163K. The transition temperature was experimentally verified via laboratory powder X-ray diffraction (Figure S3, further details in the Supporting Information) Such a change in unit cell will invariably lead to changes in carrier wavefunction overlap and hence charge transport properties. The temperature of this structural phase transition is known to be dependent on exposure to H_2O.[47] Hence it is not unreasonable to consider the possibility that the change in mobility observed in Figure 1(b) is due to such a phase transition.

To investigate the time-dependence of potential polarization mechanisms in (MA)PbI$_3$, we carried out a set of pulsed-gate measurements on a FET at various temperatures. Such dynamic measurements have proven useful to study non-idealities in FETs in the past.[48] A device identical to that illustrated in the inset to Figure 1(a) was measured using the setup illustrated in Figure 2(a). The temperature of the device was reduced to 150K, the drain current was held constant, and a pulsed voltage was applied to the gate electrode (Figure 2(b)). The source-drain current was then measured as a function of time (Figure 2(c)). We observe a fast (~5μs) rise in source-drain current (due to electronic injection) followed by a much slower decay over several seconds. The latter process is attributed to a slow polarization within the perovskite layer and an accumulation of repulsive ionic charge at the (otherwise neutral) semiconductor-dielectric interface. The capacitive nature of the planar FET architecture is known to limit the frequency response of transistors subjected to oscillatory gate voltages.[49] However this frequency is expected[49] to be many orders of magnitude higher than those under investigation in Figure 2 and this phenomenon can hence be neglected.

We observed a strong dependence of the source to drain current in FETs as a function of time and temperature. As the temperature of the FET was increased, the decay rate of the current after application of a gate bias increases substantially (see Figures 2(d) and 2(e)). This behavior is again compatible with a temperature-dependent polarization process taking place within the structure and explains why it is not possible to measure working transistors at room temperature, at normal measurement speeds. Though a number of polarization mechanisms are possible in this material, one can broadly separate these phenomena into ionic migration (which should occur on the lengthscale of the film thickness) and atomic or molecular dipole creation or alignment (which occur on an atomic/molecular lengthscale for dipole creation or microstructural lengthscale for domain alignment). In an attempt to elucidate the more likely mechanism, we carried out a set of impedance measurements on (MA)PbI_3 capacitor structures, akin to similar recent studies.[18, 21-22] The structure studied is shown in the inset to Figure 3(a). Relative permittivity was extracted from the impedance spectra using a 2-component circuit model as described in the Supporting Information, and is plotted as a function of frequency and temperature in Figure 3(a) and (b). Of note are the strong temperature- and frequency-dependence of the permittivity, and the high value in an absolute sense. The apparent permittivity is somewhat insensitive to the measurement temperature in the high-frequency regime but increases substantially with increasing temperature in the low-frequency regime. This trend is not observed in dielectric measurements of single crystals[50] and is consistent with microstructural effects in these polycrystalline thin films.[51] This behavior can be explained by two phenomena: grain boundary polarization, wherein relatively conductive grains are separated by electronically insulating grain boundaries, and space charge polarization due to ionic migration that is enhanced along grain boundaries. Both mechanisms would exhibit the observed temperature dependence, though long range ionic diffusion under an applied field would dominate at slower frequencies. Indeed, this hypothesis is consistent with the greater hysteresis observed in (MA)PbI_3 films deposited on mesoporous TiO_2,[20, 52] wherein infiltration of (MA)PbI_3 into the nanoscale pores of the TiO_2 results in nanocrystalline grains with only local structural coherence.[53] This effectively creates a multitude of pathways for facile ionic migration and a large area of inter-phase boundaries where interfacial polarization may occur. Though it is difficult to deconvolute the impact of each mechanism that contributes to dielectric relaxation, the general trend suggests that slower phenomena (e.g. proton migration or vacancy-mediated migration of the iodide anion) may be primarily responsible for the observed behavior in FET devices.[33] To ensure that this experiment is an effective probe of the (MA)PbI_3 and is not substantially perturbed by relaxation phenomena in the interfacial layers, an identical experiment was carried out on a similar structure with the (MA)PbI_3 layer omitted (see Supporting Information Figure S2). Indeed, in this simplified structure, only purely resistive behavior was observed in the frequency range of interest.

As has been suggested recently,[25, 33] if one or more ionic species in the (MA)PbI_3 structure are mobile it is not only possible that these could be relevant for device instabilities, but could also conceivably lead to favorable internal electric fields, potentially aiding charge separation and extraction. Here we have here investigated how the relative power conversion efficiency of (MA)PbI_3 photovoltaic cells change as a function of the measurement temperature. We fabricated (MA)PbI_3 photovoltaic cells in a planar architecture (inset to Figure 4(a)),[54] using the same deposition method as the FETs (See SI for more detail).[12, 43] When measured under atmospheric-pressure N_2, the devices exhibited power conversion efficiencies in excess of 9% (see Figure 4(a)). These values give us confidence that any relative PCE measurements are representative of the device itself, rather than any non-idealities. The thickness of the $MAPbI_3$ film (~100nm) has not been optimized for PV cells, and one would expect to observe higher power conversion efficiencies for a thicker film. By illuminating the device with green (530 nm) light which is well within the band gap of the material, we were able to gain an insight into how the efficiency of the device evolves with reducing temperature. Green light was chosen, rather than the full solar spectrum, to eliminate any effects of shifts in the band gap with temperature that can influence measurements with broad band illumination. In order to avoid oxidation, during the brief (~1m) exposure to air when loading samples into the cryogenic probe station, an aluminum top electrode was employed in this case, rather than a calcium/aluminum electrode, as was the case for the devices measured under N_2 (see inset to Figure 4(b)). As previously reported for a AM1.5 spectrum,[55] we see a significant reduction in the relative power-conversion efficiency of these devices as the operating temperature is reduced. Because a green light source is employed at constant intensity ($200mW/cm^2$), we have here plotted power conversion efficiency relative to the maximum value (at 245K), rather than absolute values. We see that while there is a small amount of hysteresis between reducing temperature and increasing temperature, the behavior is completely reversible. The delay between each temperature was approximately 10 minutes and we attribute the hysteresis to a lag between the temperature of the sample and that reported by the thermocouple, due to the thermal conductivity of the substrate. While the short-circuit current (J_{sc}) of the device was found to fall to about half its original value when the temperature is reduced from 300K to 160K, the open-circuit voltage (V_{oc}) increased from 0.8V at 300K to 0.9V at 160K. More details on the evolution of the device parameters are given in the Supporting Information (Section S4) and we consider the major features here. One would typically expect an ideal diode to exhibit a reducing V_{oc} with increasing temperature,[56] as observed here. The reduction in J_{sc} with reducing temperature is unlikely due to a reduction in charge generation with temperature therefore it is likely a result of recombination before charge extraction. Whether there are specific traps sites in the bulk or whether it is related to the contacts to the cell is unclear, but the effects show the largest change at the temperature where we see dramatic changes in the behavior of the FETs. This observation is consistent with our suggestion that mass-transport in the (MA)PbI_3 may not only be (at least partially) responsible for the observed instabilities in electronic devices based upon this system, but could be a contributor to the high performance of photovoltaic cells.

In summary, we have presented results from temperature dependent measurements of (MA)PbI_3 electronic devices that, when viewed collectively, suggest the existence of a substantial susceptibility to polarization at temporal and spatial scales that significantly impact the electrical behavior of the material. Many questions remain, including the details of the mechanism or mechanisms are responsible for the observed behavior, and whether and how these polarization phenomena may be advantageously suppressed (or enhanced) to improve the performance of (MA)PbI_3 thin films. Similarly, if ionic migration is responsible it is unclear as to which species are mobile, and whether it is interstitial or vacancy impurities that are responsible for the observed behavior.[22] Our work suggests that measurements of multiple types of device structures can be useful in the understanding the properties and behavior of (MA)PbI_3 and that future work on transport in field-effect devices is a fruitful complement to that on solar cells.

FIGURES

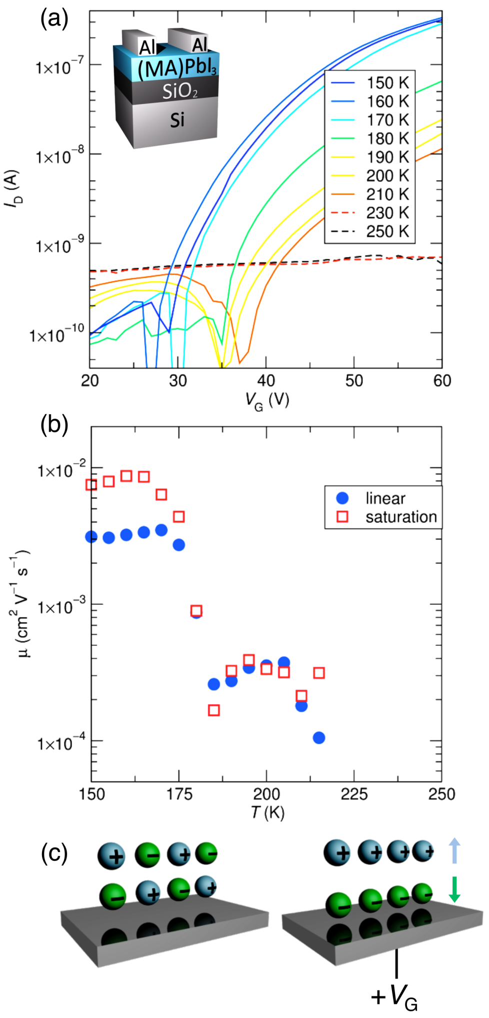

Figure 1. (a) Transfer curves (drain current as a function of gate voltage) of methylammonium lead iodide field-effect transistor measured at various temperatures between 150K and 250K. The device had a length and width of 200μm and 2,600μm respectively and a geometric capacitance of the dielectric was 23nFcm^{-2}. Inset: schematic representation of field-effect transistor structure employed in this study. Si labels the silicon gate electrode, SiO$_2$ the 150nm silicon oxide dielectric, (MA)PbI$_3$ the methylammonium lead iodide semiconductor layer, and Al the aluminum source and drain electrodes. (b) Approximated field-effect mobility evaluated using the gradual-channel approximation as a function of measurement temperature. Above 215K the measured drain current was comparable or less than the gate current and hence mobility values are not plotted for these points. (c) Schematic representation of proposed polarization mechanism of mobile ionic species in methylammonium lead iodide perovskite, under the influence of external applied gate field (V$_G$).

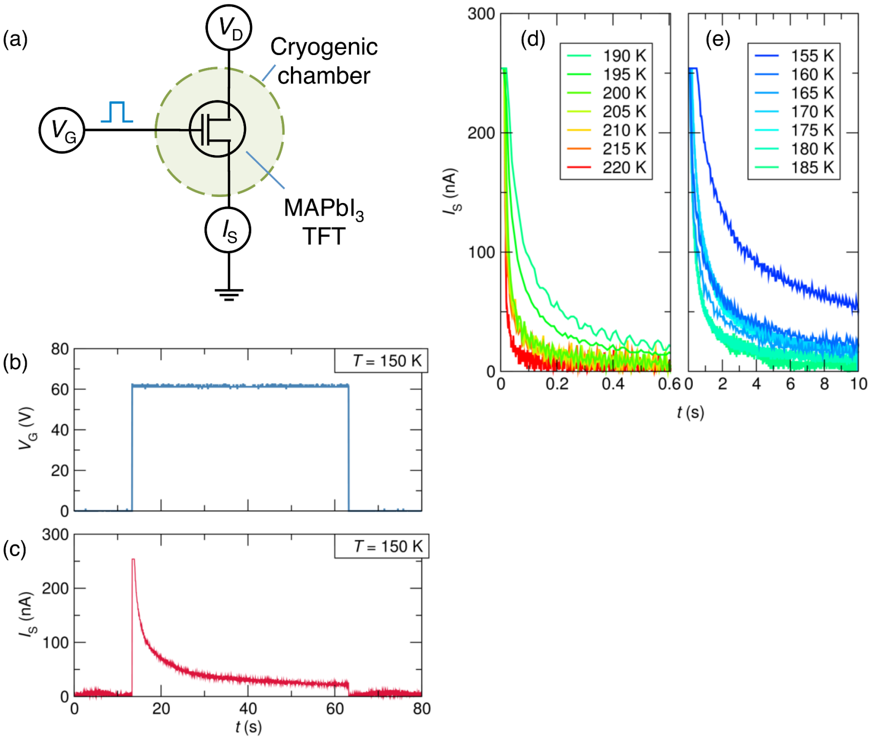

Figure 2. (a) Schematic representation of experimental setup for low-temperature, time-dependent field-effect transistor measurements. A constant voltage (V_D) is applied to the drain terminal, a pulsed voltage is applied to the gate terminal (V_G) and the source-drain current (I_{DS}) is monitored at the source terminal. (b) Gate voltage and (c) source-drain current as a function of time in methylammonium lead iodide field-effect transistor, measured at 150K. (d, e) source-drain current of methylammonium lead iodide field-effect transistor as a function of time, measured at various temperatures. The device had a length and width of 200μm and 2,600μm respectively and a geometric capacitance of the dielectric was 23 nFcm^{-2}.

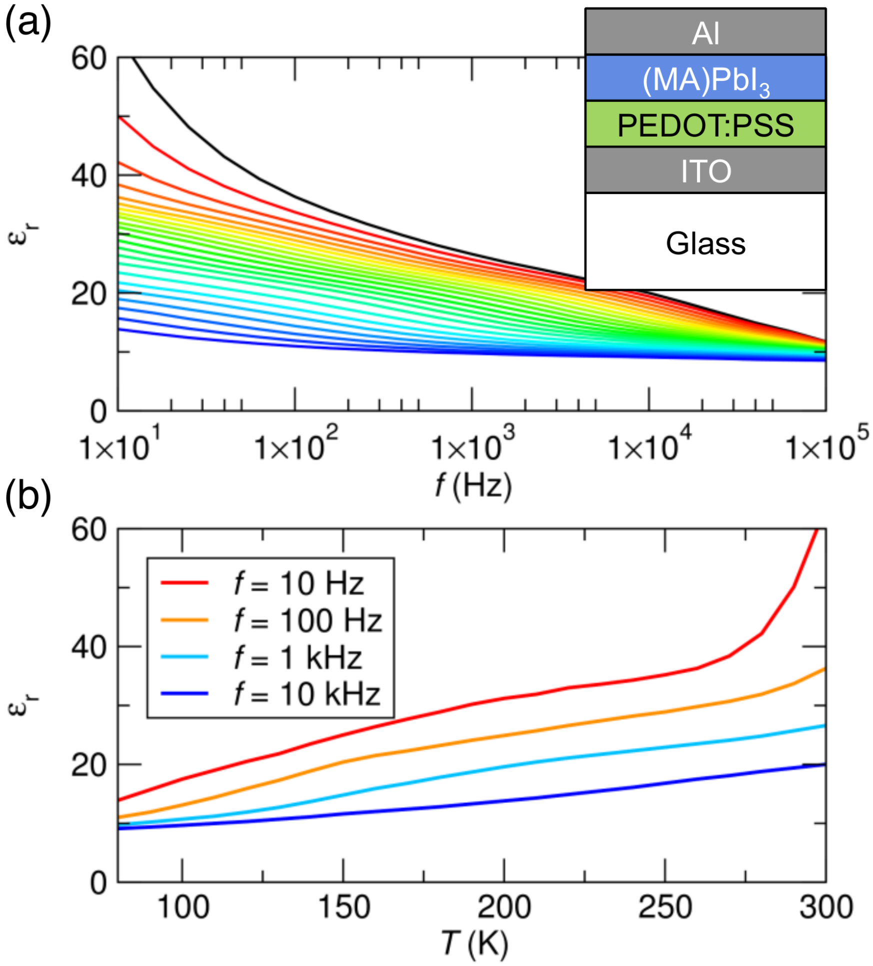

Figure 3. (a) Relative permittivity of (MA)PbI$_3$ capacitor, extracted using the 2-component circuit model described in the Supporting Information as a function of temperature, at various temperatures between 80K and 300K. Device area was 0.042 cm^2. Inset: Schematic representation of capacitor structure employed in this study. ITO labels the indium tin oxide bottom-electrode, PEDOT:PSS poly(3,4-ethylenedioxythiophene) polystyrene sulfonate, (MA)PbI$_3$ the methylammonium lead iodide semiconductor layer, and Al the aluminum top electrode. (b) The same data presented as a function of temperature for various frequencies.

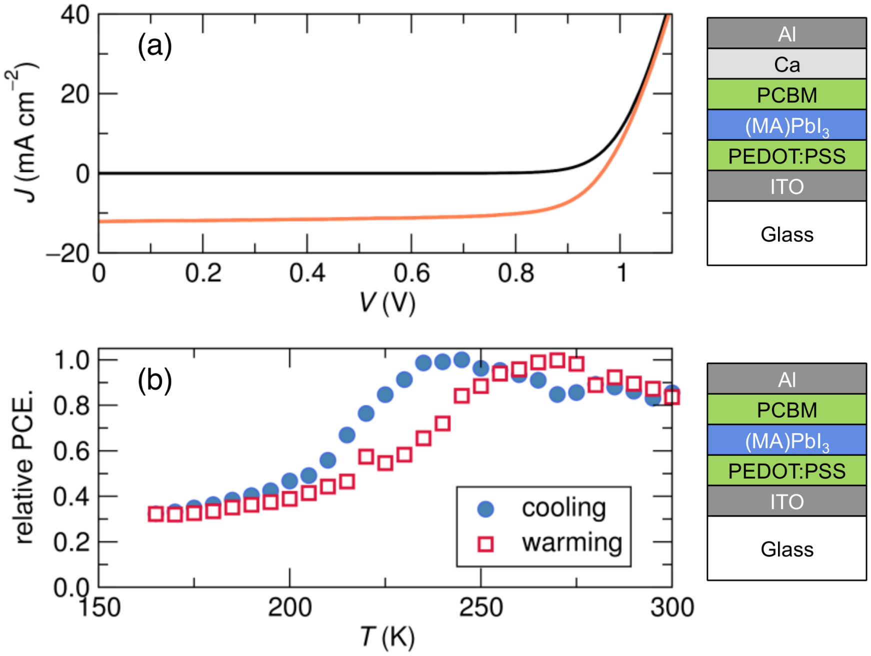

Figure 4. (a) Current-voltage characteristics of example methylammonium lead iodide photovoltaic (PV) cell with calcium / aluminum top electrode, measured in the dark and under 1 sun illumination from AM1.5 solar spectrum, under atmospheric pressure N_2. Schematic representation of PV structure employed in this study displayed alongside. ITO labels the indium tin oxide bottom-electrode, PEDOT:PSS poly(3,4-ethylenedioxythiophene) polystyrene sulfonate, $(MA)PbI_3$ the methylammonium lead iodide semiconductor layer, PCBM: Phenyl-C_{61}-butyric acid methyl ester, and Ca and Al the calcium and aluminum top electrode. (b) Relative power-conversion efficiency of methylammonium lead iodide photovoltaic cell with aluminum top electrode (structure alongside) as a function of temperature, under illumination from monochromatic green (530nm) light. Device area was $0.06cm^2$ in all cases.

ASSOCIATED CONTENT

Supporting Information. Supporting information contains details of methylammonium iodide synthesis, methylammonium lead iodide ((MA)PbI_3) thin-film preparation, field-effect transistor fabrication and measurement, capacitor fabrication and measurement, photovoltaic cell fabrication and measurement, an analysis of (MA)PbI_3 capacitor impedance spectra, an analysis of poly(3,4-ethylenedioxythiophene) polystyrene sulfonate capacitor impedance spectra and temperature-dependent powder X-Ray diffraction of polycrystalline (MA)PbI_3. This material is available free of charge via the Internet at http://pubs.acs.org.

AUTHOR INFORMATION

Corresponding Author

*Email: mchabinyc@engineering.ucsb.edu

ACKNOWLEDGMENT

This work was supported by the U.S. Department of Energy, Office of Science, Basic Energy Sciences under award number DE-SC-0012541. The UCSB-UT El Paso collaboration was supported by the NSF PREM award DMR-1205302. Partial support of the research was provided by the MC-CAM Program at UCSB sponsored by Mitsubishi Chemical Corporation (Japan). Use of the shared experimental facilities of the Materials Research Laboratory at UCSB was supported by the MRSEC Program of the National Science Foundation under Award No. DMR 1121053. J.G.L. gratefully acknowledges Virgil Elings and Betty Elings Wells for financial support through the Elings Fellowship Awards. A.J.L gratefully acknowledges support of Swiss National Science Foundation fellowship number PBSKP2-145825.

REFERENCES

1. Carlson, D. E.; Wronski, C. R. Amorphous Silicon Solar Cell. *Appl Phys Lett* **1976,** *28*, 671-673.
2. Tang, C. W. Two-Layer Organic Photovoltaic Cell. *Appl Phys Lett* **1986,** *48*, 183-185.
3. Sariciftci, N. S.; Smilowitz, L.; Heeger, A. J.; Wudl, F. Photoinduced Electron Transfer from a Conducting Polymer to Buckminsterfullerene. *Science* **1992,** *258*, 1474-1476.
4. O'Regan, B.; Gratzel, M. A Low-Cost, High-Efficiency Solar Cell Based on Dye-Sensitized Colloidal TiO_2 Films. *Nature* **1991,** *353*, 737-740.
5. Britt, J.; Ferekides, C. Thin-film CdS/CdTe Solar Cell with 15.8% Efficiency. *Appl Phys Lett* **1993,** *62*, 2851-2852.
6. Kojima, A.; Teshima, K.; Shirai, Y.; Miyasaka, T. Organometal Halide Perovskites as Visible-Light Sensitizers for Photovoltaic Cells. *J Am Chem Soc* **2009,** *131*, 6050-6051.
7. Lee, P. A.; Nagaosa, N.; Wen, X.-G. Doping a Mott insulator: Physics of High-Temperature Superconductivity. *Rev Mod Phys* **2006,** *78*, 17-85.
8. Johnston, D. C. The Puzzle of High Temperature Superconductivity in Layered Iron Pnictides and Chalcogenides. *Advances in Physics* **2010,** *59*, 803-1061.
9. Lee, M. M.; Teuscher, J.; Miyasaka, T.; Murakami, T. N.; Snaith, H. J. Efficient Hybrid Solar Cells Based on Meso-Superstructured Organometal Halide Perovskites. *Science* **2012,** *338, 643-647*.
10. Gratzel, M. The Light and Shade of Perovskite Solar Cells. *Nat Mater* **2014,** *13*, 838-842.
11. Zhou, H.; Chen, Q.; Li, G.; Luo, S.; Song, T.-b.; Duan, H.-S.; Hong, Z.; You, J.; Liu, Y.; Yang, Y. Interface Engineering of Highly Efficient Perovskite Solar Cells. *Science* **2014,** *345*, 542-546.
12. Jeon, N. J.; Noh, J. H.; Kim, Y. C.; Yang, W. S.; Ryu, S.; Seok, S. I. Solvent Engineering for High-Performance Inorganic–Organic Hybrid Perovskite Solar Cells. *Nat Mater* **2014,** *13*, 897-903.
13. Yang, W. S.; Noh, J. H.; Jeon, N. J.; Kim, Y. C.; Ryu, S.; Seo, J.; Seok, S. I. High-Performance Photovoltaic Perovskite Layers Fabricated Through Intramolecular Exchange. *Science* **2015,** *348*, 1234-1237.
14. You, J.; Hong, Z.; Yang, Y.; Chen, Q.; Cai, M.; Song, T.-B.; Chen, C.-C.; Lu, S.; Liu, Y.; Zhou, H. Low-Temperature Solution-Processed Perovskite Solar Cells with High Efficiency and Flexibility. *ACS Nano* **2014,** *8*, 1674-1680.
15. Papavassiliou, G. C.; Koutselas, I. B. Structural, Optical and Related Properties of Some Natural Three- and Lower-Dimensional Semiconductor Systems. *Synthetic Met* **1995,** *71*, 1713-1714.
16. Stoumpos, C. C.; Malliakas, C. D.; Kanatzidis, M. G. Semiconducting Tin and Lead Iodide Perovskites with Organic Cations: Phase Transitions, High Mobilities, and Near-Infrared Photoluminescent Properties. *Inorganic Chemistry* **2013,** *52*, 9019-9038.
17. De Wolf, S.; Holovsky, J.; Moon, S.-J.; Löper, P.; Niesen, B.; Ledinsky, M.; Haug, F.-J.; Yum, J.-H.; Ballif, C. Organometallic Halide Perovskites: Sharp Optical Absorption Edge and Its Relation to Photovoltaic Performance. *The Journal of Physical Chemistry Letters* **2014,** *5*, 1035-1039.

18. Dualeh, A.; Moehl, T.; Tétreault, N.; Teuscher, J.; Gao, P.; Nazeeruddin, M. K.; Grätzel, M. Impedance Spectroscopic Analysis of Lead Iodide Perovskite-Sensitized Solid-State Solar Cells. *ACS Nano* **2014,** *8*, 362-373.
19. Snaith, H. J.; Abate, A.; Ball, J. M.; Eperon, G. E.; Leijtens, T.; Noel, N. K.; Stranks, S. D.; Wang, J. T.-W.; Wojciechowski, K.; Zhang, W. Anomalous Hysteresis in Perovskite Solar Cells. *The Journal of Physical Chemistry Letters* **2014,** *5*, 1511-1515.
20. Unger, E. L.; Hoke, E. T.; Bailie, C. D.; Nguyen, W. H.; Bowring, A. R.; Heumuller, T.; Christoforo, M. G.; McGehee, M. D. Hysteresis and Transient Behavior in Current-Voltage Measurements of Hybrid-Perovskite Absorber Solar Cells. *Energy & Environmental Science* **2014,** *7*, 3690-3698.
21. Almora, O.; Zarazua, I.; Mas-Marza, E.; Mora-Sero, I.; Bisquert, J.; Garcia-Belmonte, G. Capacitive Dark Currents, Hysteresis, and Electrode Polarization in Lead Halide Perovskite Solar Cells. *The Journal of Physical Chemistry Letters* **2015,** *6*, 1645-1652.
22. Heo, J. H.; Song, D. H.; Han, H. J.; Kim, S. Y.; Kim, J. H.; Kim, D.; Shin, H. W.; Ahn, T. K.; Wolf, C.; Lee, T.-W.; Im, S. H. Planar $CH_3NH_3PbI_3$ Perovskite Solar Cells with Constant 17.2% Average Power Conversion Efficiency Irrespective of the Scan Rate. *Adv Mater* **2015**, 27, 3424-3430.
23. Ono, L. K.; Raga, S. R.; Wang, S.; Kato, Y.; Qi, Y. Temperature-dependent hysteresis effects in perovskite-based solar cells. *Journal of Materials Chemistry A* **2015,** *3*, 9074-9080.
24. Xiao, Z.; Yuan, Y.; Shao, Y.; Wang, Q.; Dong, Q.; Bi, C.; Sharma, P.; Gruverman, A.; Huang, J. Giant Switchable Photovoltaic Effect in Organometal Trihalide Perovskite Devices. *Nat Mater* **2015,** *14*, 193-198.
25. Zhang, Y.; Liu, M.; Eperon, G. E.; Leijtens, T. C.; McMeekin, D.; Saliba, M.; Zhang, W.; de Bastiani, M.; Petrozza, A.; Herz, L. M.; Johnston, M. B.; Lin, H.; Snaith, H. J. Charge Selective Contacts, Mobile Ions and Anomalous Hysteresis in Organic-Inorganic Perovskite Solar Cells. *Materials Horizons* **2015,** *2*, 315-322.
26. Yang, T.-Y.; Gregori, G.; Pellet, N.; Grätzel, M.; Maier, J. The Significance of Ion Conduction in a Hybrid Organic–Inorganic Lead-Iodide-Based Perovskite Photosensitizer. *Angewandte Chemie International Edition* **2015**, 54, 7905-7910.
27. Tress, W.; Marinova, N.; Moehl, T.; Zakeeruddin, S. M.; Nazeeruddin, M. K.; Gratzel, M. Understanding the rate-dependent J-V hysteresis, slow time component, and aging in $CH_3NH_3PbI_3$ Perovskite Solar Cells: The Role of a Compensated Electric Field. *Energy & Environmental Science* **2015,** *8*, 995-1004.
28. Niu, G.; Guo, X.; Wang, L. Review of Recent Progress in Chemical Stability of Perovskite Solar Cells. *Journal of Materials Chemistry A* **2015,** *3*, 8970-8980.
29. Nie, W.; Tsai, H.; Asadpour, R.; Blancon, J.-C.; Neukirch, A. J.; Gupta, G.; Crochet, J. J.; Chhowalla, M.; Tretiak, S.; Alam, M. A.; Wang, H.-L.; Mohite, A. D. High-Efficiency Solution-Processed Perovskite Solar Cells with Millimeter-Scale Grains. *Science* **2015,** *347*, 522-525.
30. Kagan, C. R.; Mitzi, D. B.; Dimitrakopoulos, C. D. Organic-Inorganic Hybrid Materials as Semiconducting Channels in Thin-Film Field-Effect Transistors. *Science* **1999,** *286*, 945-947.
31. Kim, H.-S.; Lee, C.-R.; Im, J.-H.; Lee, K.-B.; Moehl, T.; Marchioro, A.; Moon, S.-J.; Humphry-Baker, R.; Yum, J.-H.; Moser, J. E.; Gratzel, M.; Park, N.-G. Lead Iodide Perovskite Sensitized All-Solid-State Submicron Thin Film Mesoscopic Solar Cell with Efficiency Exceeding 9%. *Sci. Rep*. **2012,** *2, 591.*

32. Mei, Y.; Zhang, C.; Vardeny, Z. V.; Jurchescu, O. D. Electrostatic Gating of Hybrid Halide Perovskite Field-Effect Transistors: Balanced Ambipolar Transport at Room-Temperature. *MRS Communications* **2015,** 5, 297-301.
33. Eames, C.; Frost, J. M.; Barnes, P. R. F.; O'Regan, B. C.; Walsh, A.; Islam, M. S. Ionic Transport in Hybrid Lead Iodide Perovskite Solar Cells. *Nat Commun* **2015,** *6*.
34. Frost, J. M.; Butler, K. T.; Brivio, F.; Hendon, C. H.; van Schilfgaarde, M.; Walsh, A. Atomistic Origins of High-Performance in Hybrid Halide Perovskite Solar Cells. *Nano Lett* **2014,** *14*, 2584-2590.
35. Frost, J. M.; Butler, K. T.; Walsh, A. Molecular Ferroelectric Contributions to Anomalous Hysteresis in Hybrid Perovskite Solar Cells. *APL Materials* **2014,** *2*, 081506.
36. Leguy, A. M. A.; Frost, J. M.; McMahon, A. P.; Sakai, V. G.; Kochelmann, W.; Law, C.; Li, X.; Foglia, F.; Walsh, A.; O'Regan, B. C.; Nelson, J.; Cabral, J. T.; Barnes, P. R. F. The Dynamics of Methylammonium Ions in Hybrid Organic-Inorganic Perovskite Solar Cells. *Nat Commun* **2015,** *6*.
37. Beilsten-Edmands, J.; Eperon, G. E.; Johnson, R. D.; Snaith, H. J.; Radaelli, P. G. Non-Ferroelectric Nature of the Conductance Hysteresis in $CH_3NH_3PbI_3$ Perovskite-Based Photovoltaic Devices. *Appl Phys Lett* **2015,** *106*, 173502.
38. Mizusaki, J.; Arai, K.; Fueki, K. Ionic Conduction of the Perovskite-Type Halides. *Solid State Ionics* **1983,** *11*, 203-211.
39. Ishigaki, T.; Yamauchi, S.; Kishio, K.; Mizusaki, J.; Fueki, K. Diffusion of Oxide Ion Vacancies in Perovskite-Type Oxides. *Journal of Solid State Chemistry* **1988,** *73*, 179-187.
40. Iwahara, H. Oxide-Ionic and Protonic Conductors Based on Perovskite-Type Oxides and Their Possible Applications. *Solid State Ionics* **1992,** *52*, 99-104.
41. Inaguma, Y.; Liquan, C.; Itoh, M.; Nakamura, T.; Uchida, T.; Ikuta, H.; Wakihara, M. High Ionic Conductivity in Lithium Lanthanum Titanate. *Solid State Communications* **1993,** *86*, 689-693.
42. Kawakami, Y.; Fukuda, M.; Ikuta, H.; Wakihara, M. Ionic Conduction of Lithium for Perovskite Type Compounds, $(Li_{0.05}La_{0.317})_{1-x}Sr_{0.5x}NbO_3$, $(Li_{0.1}La_{0.3})_{1-x}Sr_{0.5x}NbO_3$ and $(Li_{0.25}La_{0.25})_{1-x}M_{0.5x}NbO_3$ (M=Ca and Sr). *Solid State Ionics* **1998,** *110*, 187-192.
43. Jung, J. W.; Williams, S. T.; Jen, A. K. Y. Low-Temperature Processed High-Performance Flexible Perovskite Solar Cells via Rationally Optimized Solvent Washing Treatments. *RSC Advances* **2014,** *4*, 62971-62977.
44. Sze, S. M.; Ng, K. K. *Physics of Semiconductor Devices*. Wiley: 2006.
45. Bazant, M. Z.; Thornton, K.; Ajdari, A. Diffuse-charge dynamics in electrochemical systems. *Physical Review E* **2004,** *70*, 021506.
46. Vissenberg, M. C. J. M.; Matters, M. Theory of The Field-Effect Mobility in Amorphous Organic Transistors. *Phys Rev B* **1998,** *57*, 12964-12967.
47. Baikie, T.; Fang, Y.; Kadro, J. M.; Schreyer, M.; Wei, F.; Mhaisalkar, S. G.; Graetzel, M.; White, T. J. Synthesis and Crystal Chemistry of the Hybrid perovskite $(CH_3NH_3)PbI_3$ for Solid-State Sensitised Solar Cell Applications. *Journal of Materials Chemistry A* **2013,** *1*, 5628-5641.
48. Salleo, A.; Endicott, F.; Street, R. A. Reversible and Irreversible Trapping at Room Temperature in Poly(thiophene) Thin-Film Transistors. *Appl Phys Lett* **2005,** *86*, 263505.
49. Keum-Dong, J.; Cheon An, L.; Dong-Wook, P.; Park, B.-G.; Hyungcheol, S.; Jong Duk, L. Admittance Measurements on OFET Channel and Its Modeling With R-C Network. *Electron Device Letters, IEEE* **2007,** *28*, 204-206.

50. Onoda-Yamamuro, N.; Matsuo, T.; Suga, H. Dielectric Study of $CH_3NH_3PbX_3$ (X = Cl, Br, I). *J Phys Chem Solids* **1992,** *53*, 935-939.

51. Almond, D. P.; Bowen, C. R. An Explanation of the Photoinduced Giant Dielectric Constant of Lead Halide Perovskite Solar Cells. *The Journal of Physical Chemistry Letters* **2015,** *6*, 1736-1740.

52. Heo, J. H.; Han, H. J.; Kim, D.; Ahn, T. K.; Im, S. H. Hysteresis-Less Inverted $CH_3NH_3PbI_3$ Planar Perovskite Hybrid Solar Cells with 18.1% Power Conversion Efficiency. *Energy & Environmental Science* **2015,** *8*, 1602-1608.

53. Choi, J. J.; Yang, X.; Norman, Z. M.; Billinge, S. J. L.; Owen, J. S. Structure of Methylammonium Lead Iodide Within Mesoporous Titanium Dioxide: Active Material in High-Performance Perovskite Solar Cells. *Nano Lett* **2014,** *14*, 127-133.

54. Malinkiewicz, O.; Yella, A.; Lee, Y. H.; Espallargas, G. M.; Graetzel, M.; Nazeeruddin, M. K.; Bolink, H. J. Perovskite Solar Cells Employing Organic Charge-Transport Layers. *Nat Photon* **2014,** *8*, 128-132.

55. Zhang, H.; Qiao, X.; Shen, Y.; Moehl, T.; Zakeeruddin, S. M.; Gratzel, M.; Wang, M. Photovoltaic Behaviour of Lead Methylammonium Triiodide Perovskite Solar Cells Down to 80 K. *Journal of Materials Chemistry A* **2015**.

56. Nelson, J. *The Physics of Solar Cells*. Imperial College Press: 2003.

Supporting Information

Temperature-Dependent Polarization in Field-Effect Transport and Photovoltaic Measurements of Methylammonium Lead Iodide

*John G. Labram,[1,3] Douglas H. Fabini,[2] Erin E. Perry,[1,3] Anna J. Lehner,[2,3] Hengbin Wang,[3] Anne M. Glaudell,[1] Guang Wu,[4] Hayden Evans,[2,3] David Buck,[5] Robert Cotta,[5] Luis Echegoyen,[5] Fred Wudl,[1,2,3] Ram Seshadri,[1,2,3] Michael L. Chabinyc[1,2,3]**

[1]University of California Santa Barbara, California Nanosystems Institute (CNSI), Santa Barbara, CA 93106 USA

[2]University of California Santa Barbara, Materials Research Laboratory, Santa Barbara, CA 93106 USA

[3]University of California Santa Barbara, Mitsubishi Chemical - Center for Advanced Materials, Santa Barbara, CA 93106 USA

[4]University of California Santa Barbara, Department of Chemistry & Biochemistry, Santa Barbara, CA 93106 USA

[5]University of Texas El Paso, Department of Chemistry, El Paso, TX 79968 USA

*Corresponding Author: Michael Chabinyc, Materials Department, University of California, Santa Barbara CA 93106-5050, email: mchabinyc@engineering.ucsb.edu

S1. Experimental

S1.1 Methylammonium iodide synthesis

Methylammonium iodide (CH_3NH_3I) was prepared following the common method[1] by an acid-base reaction of HI with the amine CH_3NH_2. For 2 g of product, HI (1.74 mL, 13.2 mmol, 1.05 eq., 57% in aqueous solution, 99.95%, Sigma-Aldrich) in anhydrous ethanol (2 mL, 99.5%, Sigma-Aldrich) was slowly dropped into a solution of CH_3NH_2 (1.57 mL, 12.6 mmol, 1.00 eq. 33% solution in absolute ethanol, 99%, Sigma-Aldrich) at 0 ºC. After stirring for 30 min at room temperature, the excess solvent was removed using a rotary evaporator. The remaining precipitation was recrystallized twice from a hot ethanol/water mixture and dried under vacuum at 60 ºC for 1 h to give white crystals. The phase purity was confirmed by powder X-ray diffraction.

S1.2 Methylammonium lead iodide thin-film preparation

Lead iodide (PbI_2) and CH_3NH_3I were mixed in a 1:1 molar ratio then dissolved in a mixture of dimethyl sulfoxide and γ-butyrolactone (3:7 by volume). The solution was left stirring overnight at 60°C before deposition. Films were spin-cast under atmospheric-pressure N_2 at 5,000rpm. In order to drive out solvent, chlorobenzene was applied to the sample a few seconds before the spin-casting procedure was complete, as reported elsewhere.[2-3] The films were then annealed at 110°C for 10 minutes under atmospheric-pressure N_2. CH_3NH_3I was synthesized as described in S1.1 and PbI_2 was purchased from Sigma Aldrich. Films were found to have an approximate thickness of 100nm using the above deposition technique.

S1.3 Field-effect transistor fabrication and measurement

Bottom-gate, top-contact (BGTC) field-effect transistors were fabricated on highly doped (n^{++}) wafers, acting as the common gate electrode, with a 150nm thermally grown silicon dioxide layer as the gate dielectric. The dielectric capacitance of the SiO_2 layer was 23 $nFcm^{-2}$. Methylammonium lead iodide films were deposited as described in S1.2. 60nm aluminum source and drain electrodes were deposited via thermal evaporation under high vacuum ($\sim 10^{-7}$mbar).

Static electrical characterization was carried out using two Keithley 2400 SourceMeters. Dynamic electrical characterization was carried by applying a constant voltage to the drain electrode using a Keithley 2400, and a pulsed voltage was applied to the gate electrode using a Stanford Research Systems DS345 function generator and a Krohn-hite 7600M wideband voltage amplifier. The source-drain current was measured at the source terminal with a Tektonix TDS 2014B oscilloscope, after being amplified using a Stanford Systems SR570 current preamplifier. The devices were measured under high vacuum (10^{-4} mbar) in a LakeShore cryogenic probestation. The mobility of charge carriers was estimated in the linear and saturation regime using the gradual channel approximation.[4]

S1.4 Capacitor fabrication and measurement

Capacitors were fabricated on indium tin oxide (ITO)-coated glass. poly(3,4-ethylenedioxythiophene) polystyrene sulfonate (PEDOT:PSS) was deposited onto the ITO by spin-casting at 5,000rpm in air, followed by annealing at 150°C for 10 minutes. Methylammonium lead iodide was then deposited as described in S1.2, or was omitted in the case of the data presented in S2. 100nm aluminum source and drain electrodes were deposited via thermal evaporation under high vacuum ($\sim 10^{-7}$mbar).

Impedance was measured as a function of frequency and temperature using a Solatron SI1260 impedance analyzer. The device characteristics were measured with both reducing temperature and increasing temperature. The spectra were aquired in a voltage source / current measure configuration, with a voltage input of 100 mV AC. Data were measured across the frequency range from 10 MHz to 1 Hz, with five points sampled per decade. The extracted parameters measured with reducing temperature were negligibly different from those measured with increasing temperature, suggesting any observed phenomena were completely reversible. The devices were measured under high vacuum (10^{-4} mbar) in a LakeShore cryogenic probestation.

PEDOT:PSS (AL4083) was purchased from Clevios.

S1.5 Photovoltaic cell fabrication and measurement

Photovoltaic cells were fabricated on ITO-coated glass. PEDOT:PSS was deposited onto the ITO by spin-casting at 5,000rpm in air, followed by annealing at 150°C for 10 minutes. Methylammonium lead iodide was then deposited as described in S1.2. Solutions of phenyl-C_{61}-butyric acid methyl ester (PCBM) were made in cholorbenzene (20 mg/ml) and left stirring overnight at 60°C. PCBM was then deposited onto the methylammonium lead iodide film via spin-casting at 1,500rpm under ambient-pressure N_2. The devices were then left at room temperature overnight before 100nm calcium/aluminum or aluminum top electrodes were deposited via thermal evaporation under high vacuum (~10^{-7}mbar).

Current-voltage characteristics were measured at 1 sun (AM 1.5G) under ambient pressure N_2 using a Newport xenon lamp and a Keithley 2408 source measurement unit. Characteristics were also measured under high vacuum (10^{-4} mbar) in a LakeShore cryogenic probestation using an array of high-power green (530nm) light-emitting diodes at an incident intensity of 200 W/m^2.

S2. Interpretation of (MA)PbI_3 capacitor impedance spectra

The temperature-dependent impedance spectra of an ITO/PEDOT:PSS/(MA)PbI_3/Al capacitor are shown in Figure S1. To ensure reproducibility, an additional device was fabricated and measured. This 2nd device displayed complete qualitative agreement with the first, and is omitted here for brevity (any minor differences may be ascribed to the wide variance in properties observed for materials prepared from solution at a laboratory-scale).

In the interest of minimizing assumptions in interpretation, a simple parallel resistor-capacitor (R-C) circuit is employed as an equivalent model. The impedance spectra exhibit general agreement with those expected of a parallel R-C circuit, including a flat impedance magnitude up to a corner frequency followed by a linear rolloff, and a phase that is negligible up to ~1 decade below the corner frequency, -45° near the corner frequency, and approaches -90° beyond 1 decade above the corner frequency. The parasitic series resistance and inductance (e.g. from the leads and imperfect probe contact) are only apparent above a critical frequency (here, 10^4 – 10^5 Hz) and they do not affect calculation of capacitance at slower timescales. Relative permittivities were calculated from the modeled capacitance values assuming a flat plate capacitor with an area of 4.2 mm^2 and thickness of 150 nm.

S3. Powder X-Ray diffraction of polycrystalline (MA)PbI_3

(MA)PbI_3 powder was prepared by drop-casting in ambient-pressure air from solution in dimethylformamide onto cleaned glass, evaporating solvent on a hotplate, removing material from the substrate with a razor blade, and heat treatment in a vacuum oven at 100° C to remove any residual solvent. Prior to performing XRD, the sample was ground with a mortar and pestle.

Powder X-ray diffraction was performed in a Proteum Diffractometer (transmission geometry) with a Cu anode X-ray source and an area detector. An Oxford 700 cryostream was employed for temperature actuation and control. To capture the range of $2\theta = 5° – 90°$, two images were taken at each temperature, one at low source-sample-detector angle, and one at high angle. Images were integrated using Bruker Apex II software.

FIGURES

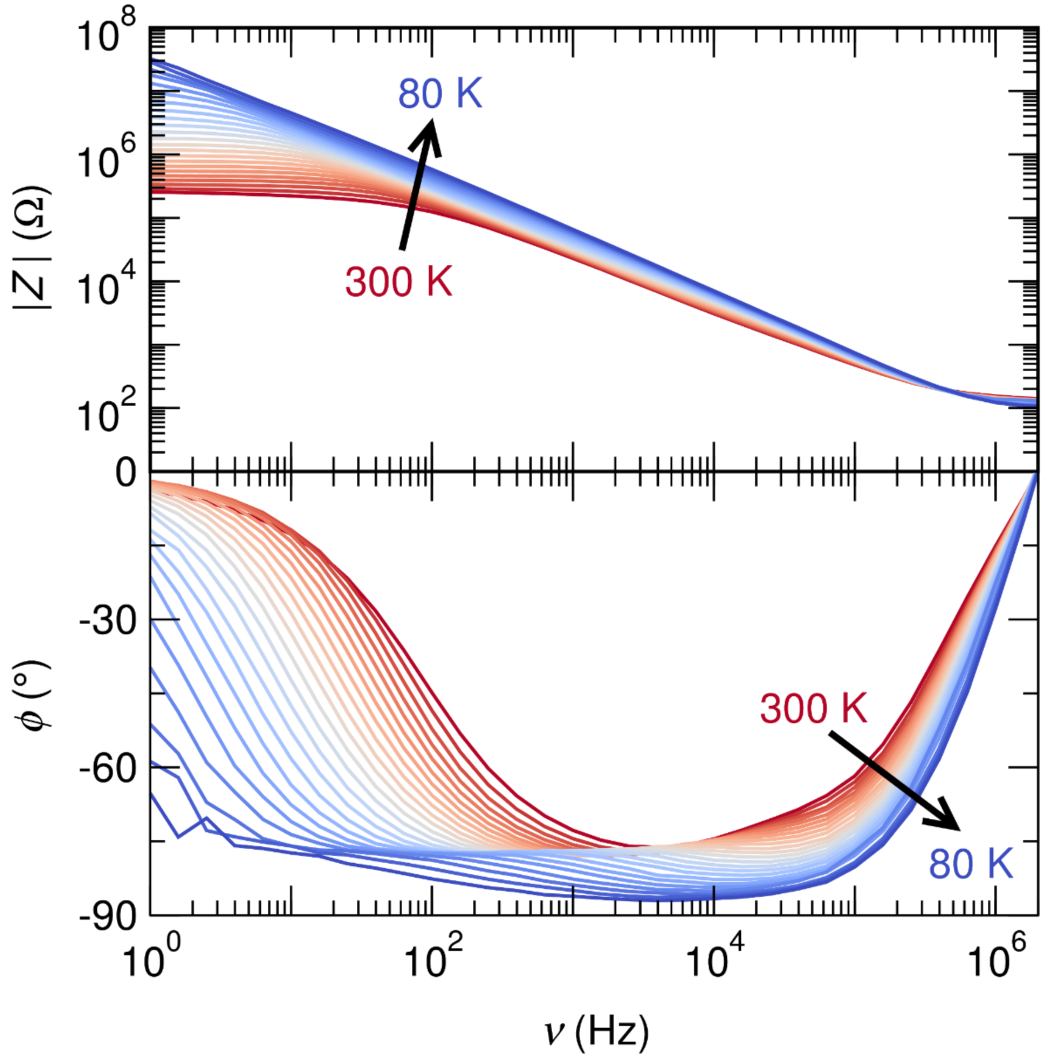

Figure S1: Impedance (top: gain, bottom: phase) spectra for ITO/PEDOT:PSS/(MA)PbI_3/Al capacitor as a function of temperature descending from 300 K to 80 K in steps of 10 K (spectra on ascending in temperature were negligibly different and are omitted here for clarity). The sharp increase and peak in impedance phase above 100 kHz is attributable to the effect of the parasitic inductance of the leads connecting the instrumentation to the probe station and the sample, as is not of concern for examining the frequency range of interest.

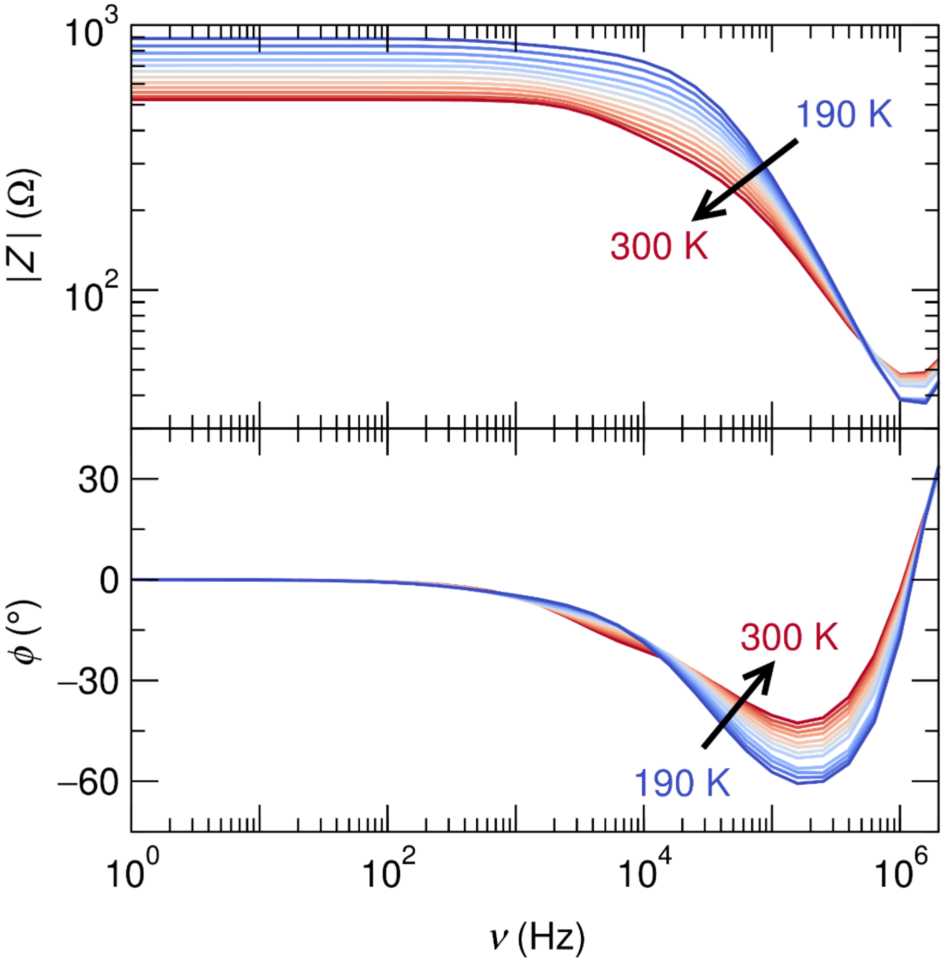

Figure S2: Impedance (top: gain, bottom: phase) spectra for ITO/PEDOT:PSS/Al device as a function of temperature ascending from 190 K to 300 K in steps of 10 K (spectra on descending in temperature were negligibly different and are omitted here for clarity). The sharp increase and peak in impedance phase above 100 kHz is attributable to the effect of the parasitic inductance of the leads connecting the instrumentation to the probe station and the sample, as is not of concern for examining the frequency range of interest.

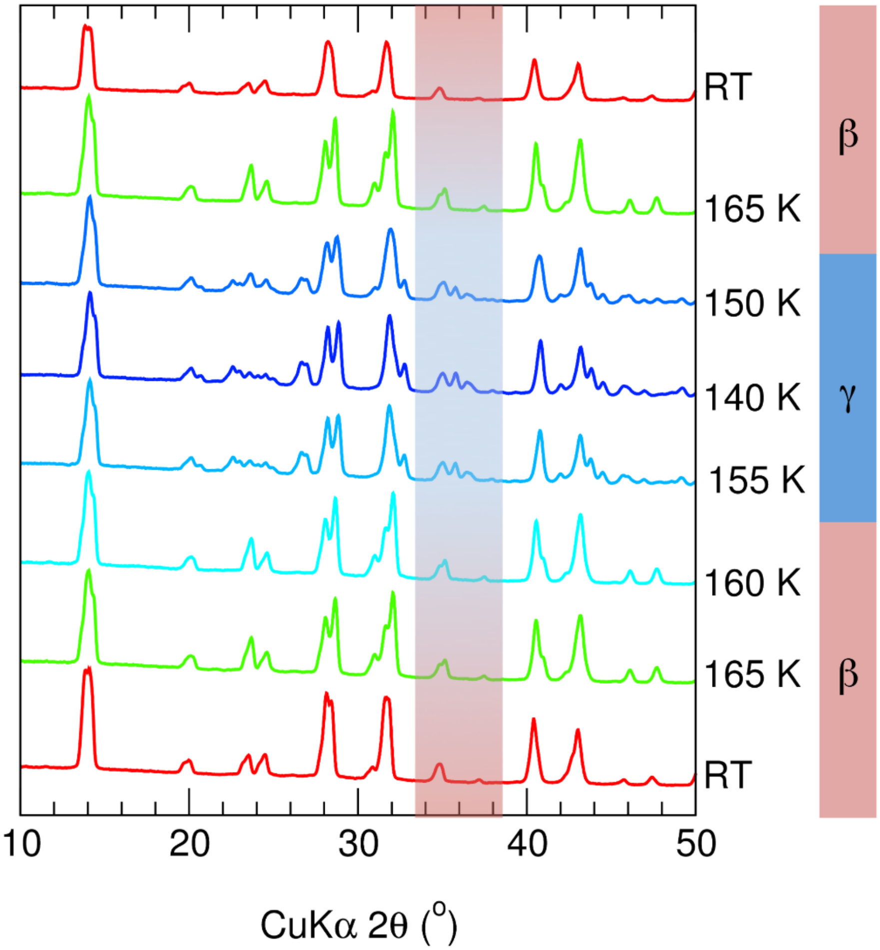

Figure S3: Powder x-ray diffraction patterns for $(MA)PbI_3$ upon descending and ascending temperature in the order R.T. - 165 K - 150 K - 140 K - 155 K - 160 K - 165 K - R.T.). Peak splitting can be observed between 155 K and 160 K indicating the first-order phase transition between the higher symmetry β phase (*I*4*cm*) and the lower symmetry γ phase (*Pnma*). With the exception of the small low-angle peak that emerges at cryogenic temperatures (possibly due to a hydrated supercell caused by sample air exposure or a trace impurity phase that is disordered at room temperature), all observable peaks are consistent with the reported structures.[4]

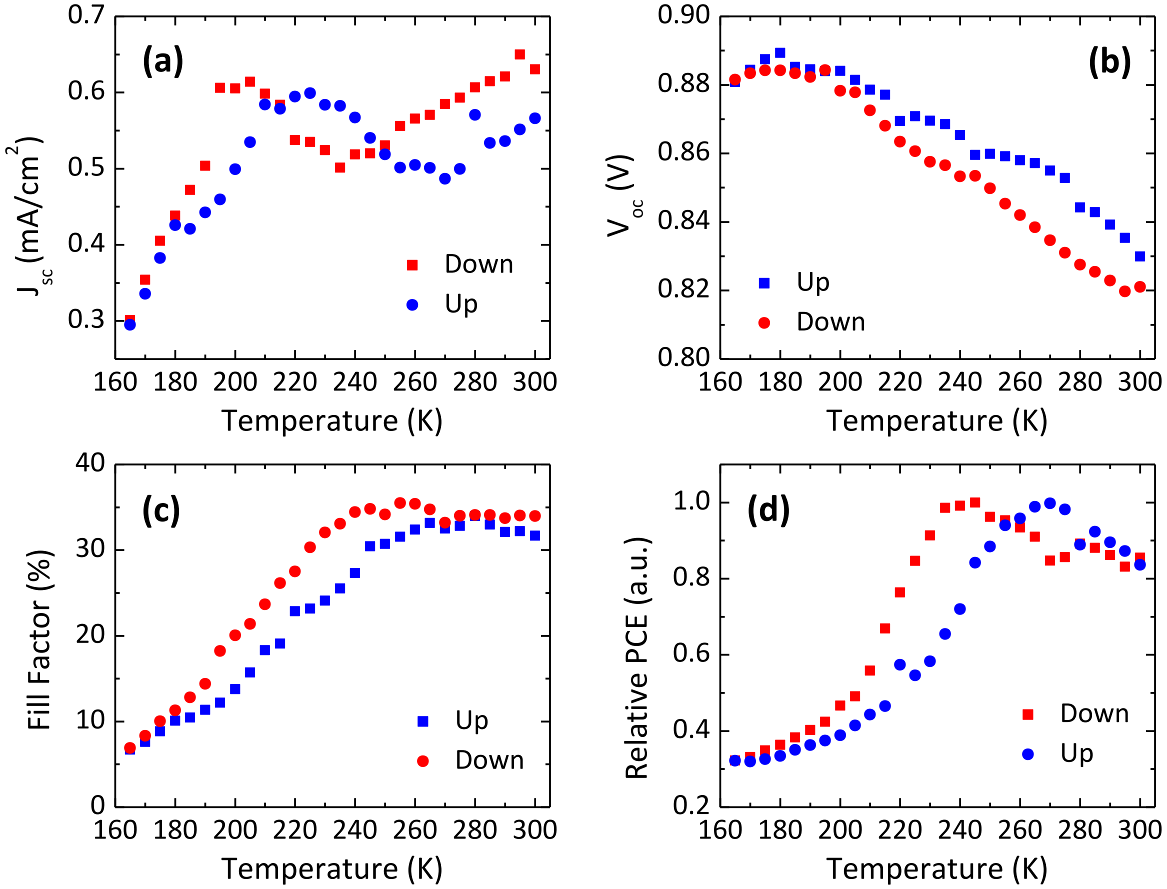

Figure S4: (a) Short-circuit current density, (b) Open-circuit voltage, (c) Fill factor and (d) relative power conversion efficiency of methylammonium lead iodide photovoltaic cell with aluminum top electrode (structure shown in inset to Figure 4(b) of main text) as a function of temperature, under illumination from monochromatic green (530nm) light. Device area was 0.06cm^2 in all cases.

REFERENCES

1. Qiu, J.; Qiu, Y.; Yan, K.; Zhong, M.; Mu, C.; Yan, H.; Yang, S. All-solid-state hybrid solar cells based on a new organometal halide perovskite sensitizer and one-dimensional TiO2 nanowire arrays. *Nanoscale* **2013,** *5* (8), 3245-3248.
2. Jung, J. W.; Williams, S. T.; Jen, A. K. Y. Low-temperature processed high-performance flexible perovskite solar cells via rationally optimized solvent washing treatments. *RSC Advances* **2014,** *4* (108), 62971-62977.
3. Jeon, N. J.; Noh, J. H.; Kim, Y. C.; Yang, W. S.; Ryu, S.; Seok, S. I. Solvent engineering for high-performance inorganic–organic hybrid perovskite solar cells. *Nat Mater* **2014,** *13* (9), 897-903.
4. Sze, S. M.; Ng, K. K. *Physics of Semiconductor Devices*. Wiley: 2006.